Biosensors and Bioelectronics 126 (2019) 470–477

Contents lists available at ScienceDirect

Biosensors and Bioelectronics

journal homepage: www.elsevier.com/locate/bios

Photothermal effects induced by surface plasmon resonance at graphene/gold nanointerfaces: A multiscale modeling study

Jiu Pang[a,b,1], Luqi Tao[a,1], Xiaoling Lu[c], Qun Yang[d], Vivek Pachauri[c], Zeping Wang[a], Sven Ingebrandt[c], Xianping Chen[a,b,*]

[a] Key Laboratory of Optoelectronic Technology & Systems, Education Ministry of China, Chongqing University and State Key Laboratory of Power Transmission Equipment and System Security, Chongqing University, Chongqing 400044, China
[b] Faculty of Mechanical and Electrical Engineering, Guilin University of Electronic Technology, Guilin, Guangxi 541004, China
[c] Institute of Materials in Electrical Engineering, RWTH Aachen University, Aachen 52074, Germany
[d] Max Planck Institute for Chemical Physics of Solids, Dresden 01187, Germany

ARTICLE INFO

Keywords:
Photothermal effects
Surface plasmon resonance
Multiscale simulation method
Sensitivity and detection accuracy
Graphene/gold nanointerface

ABSTRACT

Surface plasmon resonance (SPR) biosensors have enormous potential in biological recognitions and biomolecular interactions, especially for the real time measurement of disease diagnosis and drug screening. Extensive efforts have been invested to ameliorate the sensing performances, while the photothermal effects, which are induced by the plasmon resonance, have an obvious impact. However, due to the limitations of experimental approaches, the theoretical mechanisms and specific influences of the SPR sensors with photothermal effects are few researched. Here, a multiscale simulation method is developed to investigate the photothermal effects at graphene/gold (Au) nanointerfaces, and to calculate the quantitative contribution of the photothermal effects towards high reliability SPR sensors in order to elucidate their influence on the sensing performances by means of first-principle calculations and molecular dynamics simulations. Our results indicate that the sensitivity and detection accuracy of graphene/Au SPR sensors can be tailored from 0 K to 600 K, due to the tunable dielectric constants of Au and graphene films through temperature variation. By controlling the its material thickness, interfacial combination and lattice strain, an optimized graphene/Au SPR sensor with higher sensitivity, detection accuracy, and reliability to the temperature rising has been achieved. Such multiscale simulation method, which is capable of seeking both the role and the underlying mechanism of the interfacial phenomena, can serve as an excellent guideline for the performance optimization and commercialized application of SPR sensors in the analytical chemistry and biomedical fields.

1. Introduction

Surface plasmon resonance (SPR) based approaches are recognized across different application areas for studying molecular interactions at surfaces in highly sensitive, label-free operation and easier system-integration potential. Development of label-free assays for disease biomarkers is one such area where SPR-based sensing approaches have demonstrated immense potential. (Abadian et al., 2014; Kim and Lee, 2015; Mohammadzadeh-Asl et al., 2018; Stern et al., 2016; Zeng et al., 2014). In addition, novel platforms based on SPR are applied for detailed study of biomolecular interactions where in addition to real-time binding kinetics, alternative readout methods reveal more detailed information of biomolecular interactions at surfaces. Therefore, SPR based approaches receive immense attention for scientific and technical development and realization of sensor platforms with higher performances. Nanometer thick gold films over glass substrates form an excellent interface and have become a standard for Plasmon excitation and chemical stability for SPR applications (Stebunov et al., 2015). In recent years, deposition of thin film dielectrics on gold (Au) surfaces was exploited successfully in order to produce long-range surface Plasmon and improve SPR biosensor performance (Lahav et al., 2008; Nenninger et al., 2001). Use of thin-film dielectrics-on-Au for development of advanced SPR platform saw a significant development in the discovery of graphene – a two-dimensional (2D) material with versatile dielectric properties. Transmittance of monolayer graphene is up to 97.7% and the dielectric constants can be tuned drastically by applying

* Corresponding author.
E-mail address: xianpingchen@cqu.edu.cn (X. Chen).
[1] These authors contributed equally to this work.

https://doi.org/10.1016/j.bios.2018.11.007
Received 1 September 2018; Received in revised form 27 October 2018; Accepted 4 November 2018
Available online 06 November 2018
0956-5663/

an external electric fields which can drive charge polarizations (Iyer et al., 2014; Santos and Kaxiras, 2013; Zeng et al., 2015b). What's more, graphene tends to interact with the hydrophobic domains and π-systems of biomolecules such as DNA strands and proteins via the π-stacking. In this way, analyte-specific receptor biomolecules can be easily immobilized on the graphene surface, which is a key reason why graphene is explored as a suitable material to form a biofunctional layer for SPR sensors. Recent advances in the large-scale synthesis and substrate transfer techniques to get high-quality graphene offers an excellent opportunity to study such novel surfaces as a biofunctional layer for SPR signal enhancement (Iyer et al., 2014; Lee et al., 2008; Song et al., 2010).

The sensing performance in SPR sensors strongly depends on the thickness and dielectric constant of the functional layers in SPR sensors (Singh et al., 2015). Here, graphene with varying layers, graphene oxide, reduced graphene oxide, or graphene–MoS2 hybrid structures have attracted extensive efforts to ameliorate the sensitivity of SPR signals and improve the sensing performances (Amendola, 2016; Miao et al., 2015; Wang et al., 2016; Xue et al., 2014; Zeng et al., 2015a). In addition, the sensing performances have been confirmed to be influenced by the temperature (Qiu and Wei, 2014). Wei *et al.*(Qiu and Wei, 2014) discovered that the temperature at the metal/dielectric nanointerfaces was raised to above 500 K. It was shown that, the electromagnetic energy is released via heat dissipation when Plasmon resonance occurs, raising the temperature of the Au/dielectric nanointerfaces. Furthermore, Qiu *et al.*(Chen et al., 2012) found that the temperature of the Au nanoparticles with a nanosecond pulsed light irradiation was raised to above 795 K for the strong plasmonic resonance. These temperature related changes at the interface also alter the composition of biomolecular layer affecting molecular absorption/desorption rates (Raether, 1988; Reimhult et al., 2003; Röntzsch et al., 2007; Roper et al., 2007). Therefore, the much lower power light sources ($\sim mW/mm^2$) were recommended to be used in order to reduce the photothermal effects (Galvez et al., 2017). Temperature correction methods were also proposed, such as temperature stabilization, compensation, and multi-channel design methods, to attenuate the influences of the photothermal phenomenon (Naimushin et al., 2003a; O'Brien et al., 1999; Taylor et al., 2006; Zhao et al., 2015). Variation in optical properties by temperature related changes are expected to influence Plasmon resonance curves, signifying that the sensitivity and detection accuracy of SPR platforms require a detailed relook into estimation of their sensor performance. At present, efforts to understand theoretical mechanisms, photothermal influences, and optimum temperatures are urgently required to intensify development of new-age SPR approach and optimization for real applications.

In this work, we propose a multiscale simulation method the using density functional theory and molecular dynamics to explore the theoretical mechanisms and quantitative photothermal influences in graphene/Au SPR sensors. In doing so, we establish the relationship between the temperatures and the dielectric constants of Au and graphene films. The results show that the rising temperatures have different influences on both (cubic and triclinic) Au and (AA-stacking, AB-stacking, and monolayer) graphene structures. The sensing performance of this SPR platform with graphene/Au nano-interfaces was then analyzed with change of layer thicknesses and dielectric constants. We found that the sensitivity and detection accuracy of graphene/Au SPR sensors could be tailored between temperatures ranging from 0 K to 600 K. Additionally, the AA-T and 1L-T graphene/Au stacked SPR systems possessed higher sensitivity, detection accuracy and controllability under strong photothermal effects. The methods and results presented in this work are expected to have further impact towards the understanding of SPR phenomena at metal-2D material interfaces and significantly influence the realization and optimization of advanced SPR platforms for analytical chemistry and biomedical applications.

2. Methods

We used the first-principles method to calculate the stable Au and graphene structures and dielectric constants. Total first-principle calculations were carried out with the Vienna Ab initio Simulation Package (VASP) (Kresse and Furthmüller, 1996). The projector augmented wave (PAW) method was selected to describe the core electrons and the Perdew Burke Ernzerhof (PBE) was used for the exchange-correlation term (Blöchl, 1994). The cutoff energy of the plane wave basis used for the valence orbitals was 600 eV. The Au and graphene bulk structures were optimized using a k-sampling grid within a Monkhorst-Pack scheme of 14 × 14 × 14. Two lattice types (cubic and triclinic) of the Au structure, which were downloaded from the Materials Project Database (http://www.materialsproject.org), were taken into account (Jain et al., 2011). The AA-stacking and AB-stacking graphene models of multilayer graphene structures were constructed and optimized with lattice parameters of 2.44 × 2.44 × 3.16 Å and 2.44 × 2.44 × 5.96 Å, and in agreement with previous studies (Flores et al., 2009; Saha et al., 2008; Xu et al., 2010). Additionally, the 1 layer to 6 layers graphene models were built and calculated with a 14 × 14 × 1 k-point grid. The geometric configurations of the few-layer graphene were periodic in the xy plane and separated by 50 Å along the z direction to avoid spurious interactions between the adjacent sheets. The geometry relaxations using the conjugate method were not finished until the energies of the convergence level on each ion were less than 10^{-6} eV. All the atom coordinates and lattice lengths were relaxed until the maximum force was less than 0.001 eV/Å.

Molecular dynamics were utilized to calculate the thermal expansion coefficients (TEC) of the Au film in SPR sensors. The LAMMPS package and the embedded atom model (EAM) were chosen for Au calculations (Foiles et al., 1986; Plimpton et al., 2007). The EAM potential is appropriate to use for the precise description of the systems at this size and time scale (Liu et al., 1991). In particular, the EAM potential for the Au structure is quite accurate, well developed, and has been studied extensively (Foiles et al., 1986; Liu et al., 1991; Nelson et al., 1989). The Au molecular dynamics models were constructed by expanding the Au cubic and triclinic unit cells. The Au supercell models were first relaxed at 0 K, and then the stable models were used for the heating simulations. The NPT molecular dynamics simulations were carried out with Nose−Hoover thermostat chains (Melchionna et al., 1993). The time step of the motion equations was 0.0001 ns and the total time was 5 μs, which guaranteed the accuracy of the results (Liu et al., 1991; Nelson et al., 1989; Süle et al., 2014; Yue et al., 2017). The total time was long enough to obtain the preferable balanced systems.

3. Results

The Au films in the SPR sensors are approximately 500 Å, which insures that the SPR sensors possess high detection accuracy (Kumar Maharana et al., 2013; Maharana and Jha, 2012; Schasfoort, 2017). Accordingly, the Au structures were calculated to obtain the dielectric constants of the Au films. The Au cubic and triclinic structures (from the Materials Project Database) are shown in Fig. 1(A) and (B). The lattice parameters of the Au cubic structure are 4.17Å × 4.17Å × 4.17Å. The lattice parameters of the Au triclinic structure are 2.93Å × 2.93Å × 4.90Å and the gamma angle is 120°.

In Fig. 1(A) and (B), we present the dielectric constant curves of Au structures along the z-axis direction. The solid blue and dotted red curves represent the real and imaginary parts of the dielectric constants, respectively. The dielectric constant curves exhibit large fluctuations between 200 nm and 800 nm and tend to be more flat between 800 nm and 1400 nm. The real and imaginary parts are -30.6 and 3.79 (-27.6 and 4.05) for the Au cubic (triclinic) structure under 780 nm wavelength light irradiation. These results are very close to the experimental data (-29.02 and 2.027) that was extracted from the handbook on the optical constants of metals (Adachi, 2012).

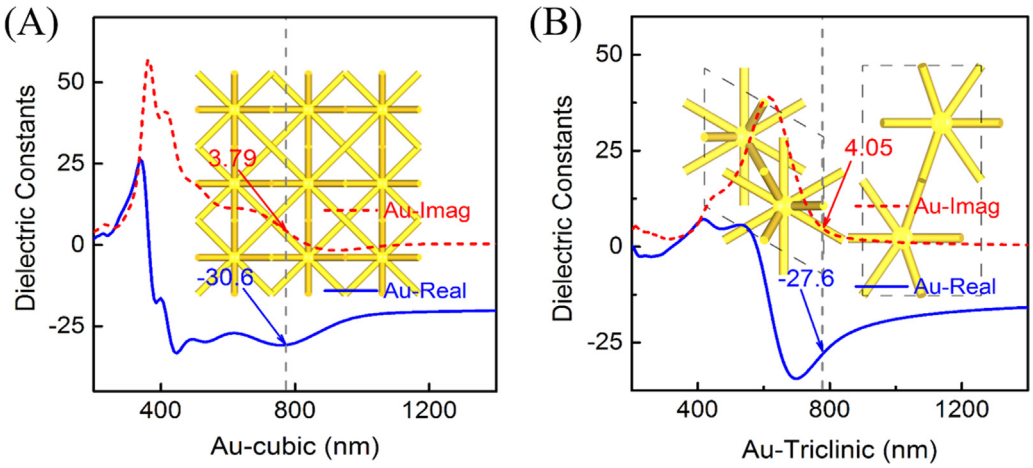

Fig. 1. Crystal structures and dielectric constant curves of (A) cubic and (B) triclinic Au unit cells at 0 K. The specific dielectric constants under 780 nm incident light are labeled.

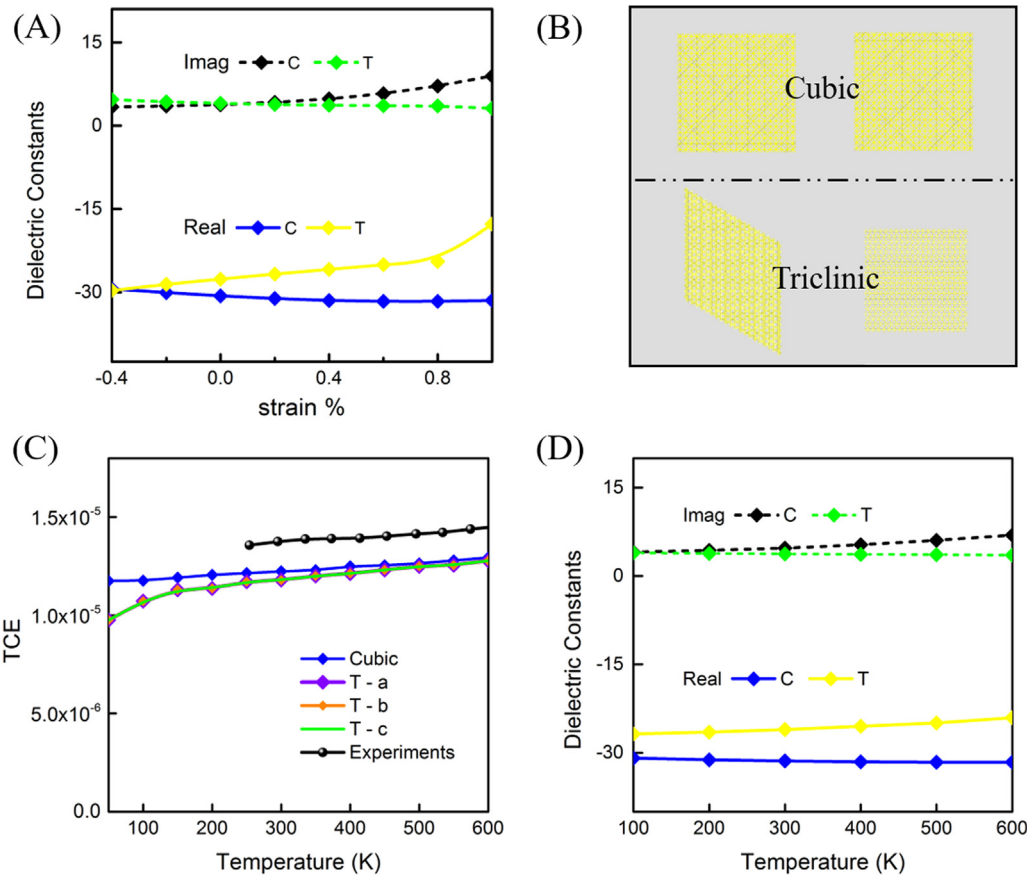

Fig. 2. (A) Strain-Dielectric constant curves of the Au structures at 0 K. (B) Au cubic and triclinic supercell models. (C) Simulations and experimental results of the TEC. (D) Temperature-Dielectric constant curves of the Au films. C and T represent the cubic and triclinic Au structures, respectively. All of the dielectric constant values are under the light wavelength of 780 nm.

As the effects of lattice strain on optical properties have been discussed in many works, we realize that the lattice deformations induced by photothermal heating can result in optical parameter variations (Çakır et al., 2014; Quereda et al., 2016; Tan et al., 2016; Yang et al., 2015). Therefore, the dielectric constants of Au structures with different lattice strains (from -0.4% to +1.0%) were calculated, as shown in Fig. 2(A). Surprisingly, the dielectric constant curves of the Au cubic and triclinic structures displayed opposite tendencies, with the strain increasing in both the real and imaginary parts. For the real parts, the dielectric constant values were equal (nearly -29.5) when the strain was -0.4%. With the increase of the strain, the real parts of the Au cubic structure declined, while the real parts of the Au triclinic structure increased. The disparity of the real parts finally surpassed 13, indicating that the cubic and triclinic structures possessed distinct optical properties with the increase of the strain. For the imaginary parts, the dielectric constant curves intersect when the strain is + 0.1%. The imaginary part of the curve of the Au cubic structure continues to increase with the increasing strain and it becomes two times larger than the imaginary part of the curve of the primary Au cubic structure without lattice strain. However, the imaginary part of the curve of the Au triclinic structure remains steady with the lattice strain.

The lattice deformation could then represent the structure expansion or contraction under different temperatures. We then calculated the thermal expansion coefficients (TEC) of the Au bulk structures and

thus the lattice parameters at different temperatures could be computed. As shown in Fig. 2(B), two large Au supercells, including $10 \times 10 \times 10$ cubic cells (4000 atoms) and $20 \times 20 \times 10$ triclinic cells (8000 atoms), were constructed. The TEC obtained from the molecular dynamics simulations were approximately equal between 150 K and 600 K, as shown in Fig. 2(C). The results were very close to the experiment data, with only a small disparity of about 0.1×10^{-5} K^{-1} (Nix and MacNair, 1941). In this way, we linked the relationship between the temperatures and dielectric constants with the following equations:

$$L_{strain} = L_{Temp} = L_{0K} \times (1+Temp \times TEC) \quad (1)$$

The lattice parameters at the specified temperatures (L_{Temp}) were computed using the initial lattice parameters (L_{0K}) and *TEC* values. The relationship between the L_{Temp} value and the lattice parameters with strains (L_{strain}) was determined.

$$DC_{strain} \xrightarrow{TEC} DC_{Temp} \quad (2)$$

Finally, the dielectric constants (DC_{strain}) were calculated using the DFT method for the appointed L_{strain} values that were related to the temperatures. Thus, the optical properties of Au structures with specific lattice deformations could roughly represent the optical properties of the Au layers under different ambient temperatures (larger than 0 K). The temperatures and dielectric constants curves at 780 nm were also obtained, as shown in Fig. 2(D).

The real part of the dielectric constant for Au cubic structure decreased slightly (-31.60) when the temperature was increased up to 600 K. An opposite effect was seen for Au triclinic structure with an increase (-24.05) with increase in temperature. The imaginary part of dielectric constant for Au cubic structure, however, increased (6.95) with rise of the temperature. For Au triclinic structure, the imaginary parameter decreased slightly (3.55) with increase in temperature. These unique trends in the change of dielectric parameters with change of temperature are expected to have critical effect on the sensing performance of graphene/Au SPR sensors. The analyses of the sensor performance using diverse interfacial combinations, varied dielectric constants and lattice deformations are discussed later in this paper.

Now we approach the 2D functional layers in SPR sensors, where the layer thickness is reported to critically influence on the plasmon resonance conditions (Falkovsky, 2008; Falkovsky and Pershoguba, 2007; Santos and Kaxiras, 2013). It was reported that the sensitivity to changes in refractive index denoted as S_n (defined as **Eq.** 3) starts to decrease when the thickness of the graphene film is higher than 8 nm (Stebunov et al., 2015). Overall, layer thicknesses between $5 \sim 10$ nm are reasonable for an excellent sensing performance of the SPR sensors (Stebunov et al., 2015; Xue et al., 2013). However, such a large-scale molecule model is not proper for first-principles calculations (the models can only contain about 100 atoms). In addition, since the dielectric constants vary as the number of graphene layers increases (Santos and Kaxiras, 2013), the optical property results of few-layer graphene cannot precisely represent the optical properties of graphene films (dozens of layers).

Thus, in order to calculate the optical properties of the graphene based functional layer, we used AA-stacking and AB-stacking mode graphene bulk structures, representing the multilayer graphene (8 nm) films. For AA-stacking mode graphene, as shown in Fig. 3(A), the real and imaginary parts of the dielectric constants were 3.25 and 0.0045, respectively. For 780 nm wavelength light, the dielectric constant curves of AA-stacking mode graphene tended to be flat, while those of the AB-stacking mode graphene, as shown in Fig. 3(B), had large ripples and the real part was negative (-0.856) at 780 nm. Additionally, the imaginary part of the AB-stacking mode graphene was much larger (4.60) than that of the AA-stacking mode graphene (0.0045). The large imaginary parts had a strong influence on the sensing performance of the SPR sensors. Moreover, the dielectric constant curves of monolayer (1 L) graphene were smooth between 200 nm and 1400 nm, as shown in Fig. S1. The real and imaginary parts of the dielectric constants were 1.1015 and 0.0002, respectively.

As discussed above, we have established the relationships between the temperatures and dielectric constants of Au films. Then, we calculated the dielectric constants under the specified strains based on Eqs. (1) and (2) to obtain the temperature-dielectric constant curves of the graphene films. In recent years, several theoretical and experimental works have studied the TEC values of graphene using various methods, such as the methods used by the UK nuclear industry, UCAR Carbon Company Inc, JAERIM, etc (Calizo et al., 2007; Morgan, 1972; Mounet and Marzari, 2005; Pavone et al., 1993; Tsang et al., 2005; Yoon et al., 2011; Zakharchenko et al., 2010). Nevertheless, some discrepancies were present among these results and the deviations were not perfectly disposed. In this paper, the TEC values of graphene films are quoted from the previous research (Tsang et al., 2005). The real part and imaginary part variations of the AA-stacking, AB-stacking, and 1 L graphene under different temperatures are plotted in Fig. 3(C) and (D). For the AA-stacking mode graphene, the imaginary part was unchanged while the real part decreased with the rising temperature. For the AB-stacking mode graphene, the imaginary part dropped rapidly while the real part increased. Furthermore, the dielectric constant variations of the 1 L graphene were less than 0.001 for temperature between 0 K and 600 K. Therefore, the influences of the photothermal effects on the 1 L graphene, AA-stacking and AB-stacking multilayered graphene were gradually enhanced.

In addition, as shown in Fig. 3(E) and (F), we calculated the dielectric constants of AA-stacking few-layer graphene from 1 layer to 6 layers, and of 2, 4, 6 layers of AB-stacking few-layer graphene. For the AA-stacking few-layer graphene, the dielectric constants gradually increased with the increase of the graphene layers and finally reached 3.25 (real) and 0.0045 (imaginary). For the AB-stacking few-layer graphene, the imaginary part curve kept growing and it reached 4.60 for the bulk graphene, while the real part slowly increased and finally dropped to -0.8. These results were subsequently used for the analysis of the plasmon resonance curves and the sensing performances.

The detection performances of the SPR sensors were mainly determined by the total sensitivity (S) and detection accuracy (D_n) (Maharana and Jha, 2012). First, S was defined as the ratio of the variation of the output signal to that of the measurement quantity (Homola, 2003). For general SPR sensors based on Kretschmann's theory, the output signal is the resonance angle θ and the measuring quantity is the analyte solution concentration C (Kretschmann, 1971). Thus, S is defined by the following formula:

$$S = \frac{\Delta\theta}{\Delta C} = \frac{\Delta\theta}{\Delta n} \times \frac{\Delta n}{\Delta C} = S_n \times E \quad (3)$$

In the formula, the Δn is the refractive index variation, and Δn is taken as 0.005° for modeling (Maharana and Jha, 2012; Stebunov et al., 2015). Thus, S can be converted to the refractive index sensitivity (S_n) and the detection efficiency (E). S_n is defined as the ratio of the resonance angle variation ($\Delta\theta$) to Δn. E is determined by the reaction characteristics between the analyte molecules and biofunctional layers (Pang et al., 2017; Stebunov et al., 2015; Yang et al., 2016). Moreover, E is proportional to the adsorption site quantities on the sensing interface $E \propto N_{ad}$. However, due to the limitations of the density functional theory and the molecular dynamics simulations, it is almost impossible to establish a large-scale system that includes the antigens, antibodies, and biofunctional layers. Fortunately, due to the small temperature fluctuations of the solutions, the molecular absorption/desorption rate and quantity variations will be minimal. Second, D_n is defined with the following formula:

$$D_n = \frac{1}{FWHM} \quad (4)$$

The FWHM term represents the full width at half minimum of the SPR curves. A small FWHM value results in a high D_n value, which

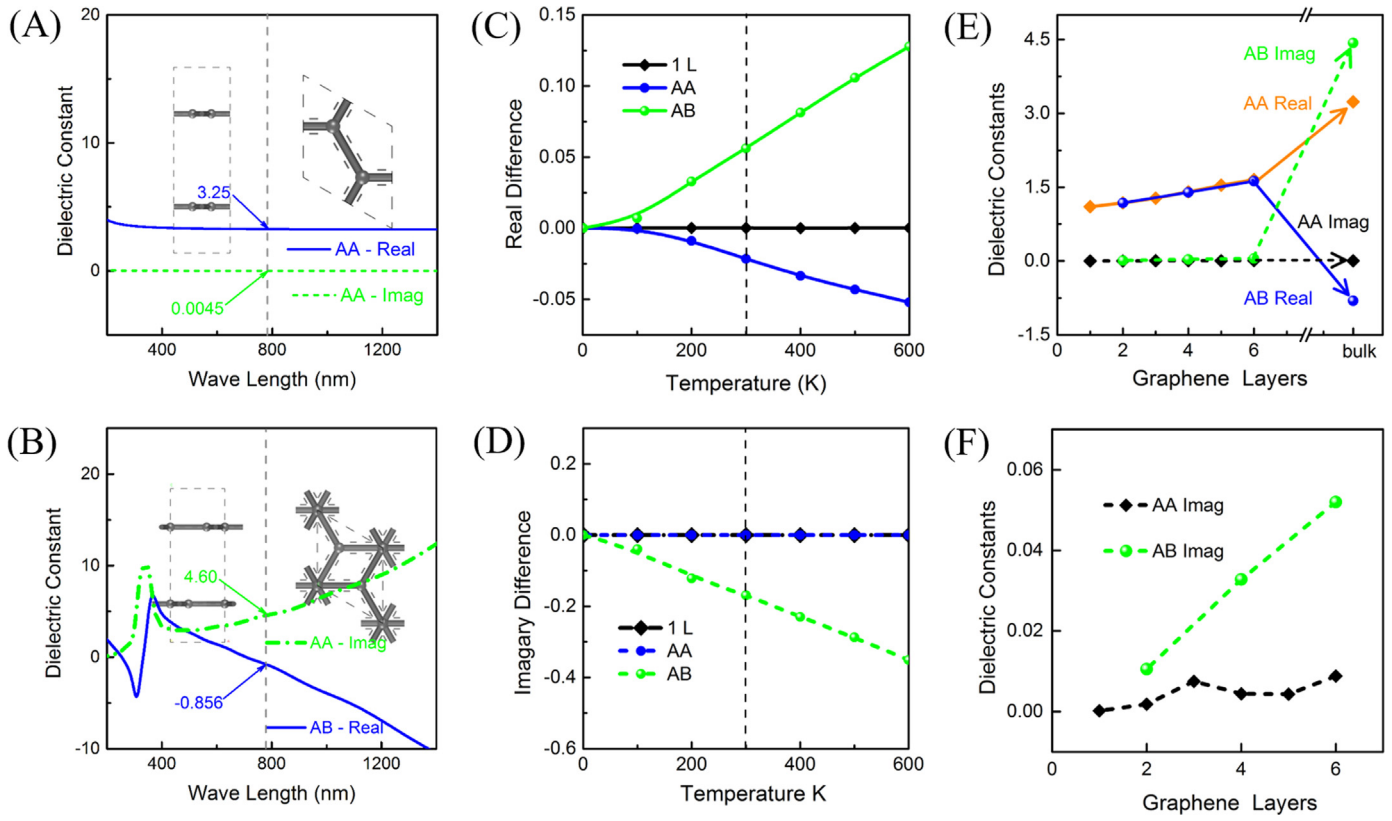

Fig. 3. Dielectric constant curves and the crystal structures of (A) AA-stacking and (B) AB-stacking mode graphene. The (C) real part and (D) imaginary part variations with rising temperatures. (E, F) Dielectric constants curves of few-layer graphene with the increasing thicknesses.

means that the measurement of the resonance angle is accurate. In short, to search for high sensing performance biofunctional materials, the E, S_n, and D_n parameters of the SPR sensors should be regarded as important.

Then the SPR curves of the graphene/Au SPR sensors under 300 K were calculated by the WinSpall software program (Liu et al., 2018). Detailed input parameters for the SPR curve calculations of the different graphene/Au stacked modes are listed in Table S1. The corresponding SPR curves are plotted in Fig. 4(A). The AA, AB, and 1 L labels represent the AA-stacking, AB-stacking, and single layer graphene, respectively. The C and T labels represent the Au cubic and triclinic structures. Additionally, each S_n and D_n value of the six stacked types of the SPR sensors was calculated, as shown in Fig. 4(B). The grey-edged bars represent the S_n values and the bars without the edge colors represent the D_n values.

For the 1L-C stacked system, the S_n value was 98 deg/RIU and the D_n value was 0.56/deg, which has the highest detection accuracy of all the graphene/Au stacked systems. For the AA-C stacked systems, the S_n value was 101 deg/RIU and the D_n value was 0.48/deg. For the 1L-T stacked system, the S_n value was 99 deg/RIU and the D_n value was 0.48/deg, and we found that AA-C and 1L-T stacked systems had the similar sensitivities and detection accuracies. For the AA-T stacked system, the S_n value was 106 deg/RIU and the D_n value was 0.39/deg. Furthermore, the D_n values of the AB-C and AB-T stacked systems were very low (~0.1/deg), indicating that the AB-stacking mode graphene structure may not be appropriate for use as a biofunctional film. The low detection accuracy, mainly resulting from the large imaginary parts of the dielectric constants, was expected to make the measurement results inaccurate. Consequently, we determined that the use of the AA-T, AA-C, 1L-T, and 1L-C stacked systems was satisfactory for obtaining a

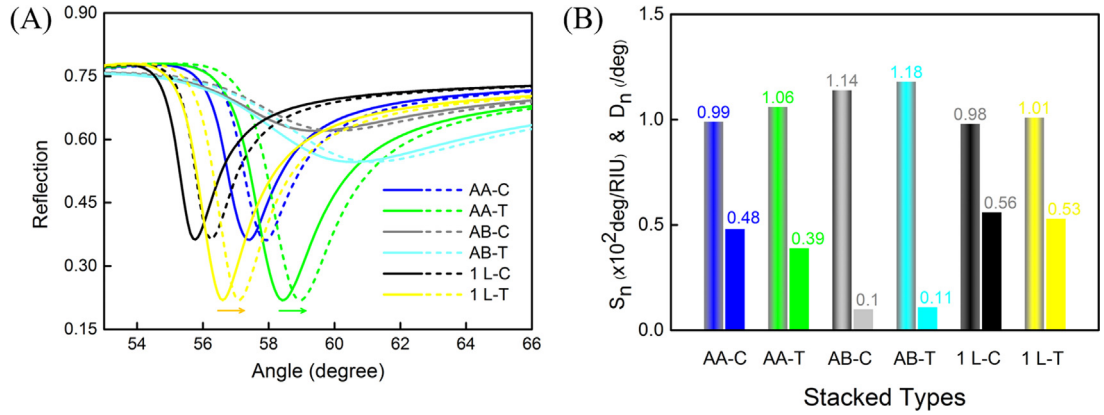

Fig. 4. (A) SPR curves of the AA-C, AA-T, AB-C, AB-T, 1L-C, and 1L-T Graphene/Au stacked SPR systems. (B) The grey-edged bars represent the S_n values, and the bars without edge colors represent the D_n values.

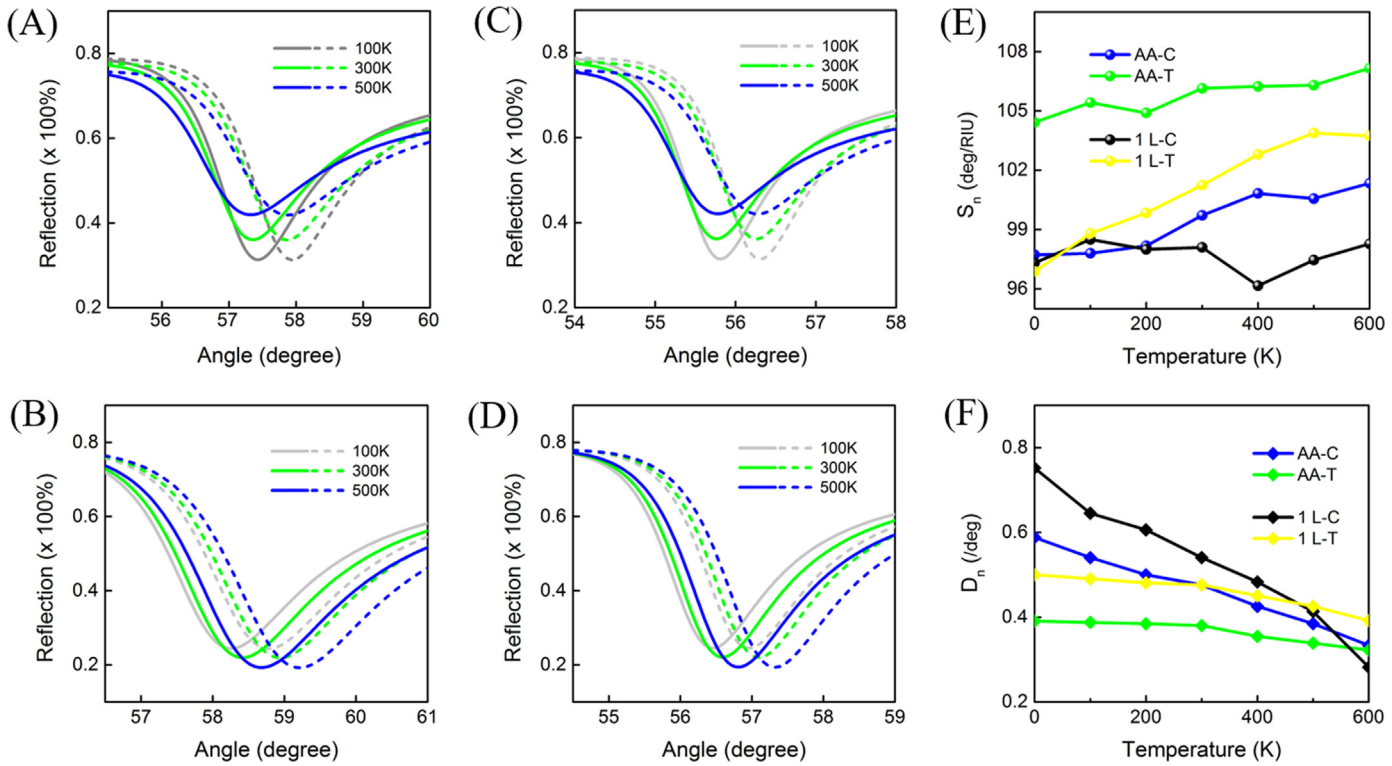

Fig. 5. The SPR curves of the (A) AA-C, (B) AA-T, (C) 1L-C, and (D) 1L-T stacked systems in different temperatures and the corresponding (E) S_n and (F) D_n variation curves.

high sensitivity and detection accuracy SPR sensor at room temperature.

Furthermore, the detection performances of the SPR sensors are influenced by temperature effects. As shown in Fig. 5(A-D), the SPR curves of the AA-C, AA-T, 1L-C, and 1L-T stacked systems ranging from 0 K to 600 K were calculated. For the AA-T and 1L-T stacked systems, the plasmon resonance shifts ($\Delta\theta$) induced by the photothermal effects were the same order of magnitude as the $\Delta\theta$ shifts induced by the biomolecules, indicating that the influences of the photothermal effects were significant. Since the photothermal effects increase the temperature of the graphene/Au nanointerfaces, our main attentions should be focused on the 300≃600 K temperature regions. We found that the $\Delta\theta$ from 500 K to 600 K was larger than that from 300 K to 500 K, which was due to the different change quantities of the dielectric constants at different temperature stages. In addition, the S_n and D_n curves of the AA-T, AA-C, 1L-C and 1L-T graphene/Au stacked systems are integrated and shown in Fig. 5(E) and (F). We found that the AA-T stacked system had the highest sensitivity from 0 K to 600 K. The S_n values of the AA-T, 1L-T and AA-C stacked systems increased, while that of the 1L-C stacked system was not sensitive to the temperature variations. Additionally, the D_n values of the four stacked systems all declined with the rising temperature, as shown in Fig. 5(F). The declines were slower for the AA-T and 1L-T stacked systems, while that of the 1L-C stacked system quickly dropped from 0.75/deg to 0.28/deg and that of the AA-C stacked system decreased from 0.59/deg to 0.33/deg. We predict that the D_n value of the 1L-C and AA-C graphene/Au stacked systems would continue to decrease to a much lower value than that of the 1L-T and AA-T stacked systems, with temperatures over 600 K. We conclude that the sensitivities increased in all systems, yet the detection accuracies declined with the enhancement of the photothermal effects. As a result, it was determined that the AA-T and 1L-T stacked graphene/Au SPR systems possessed a large available temperature range and an excellent sensing performance with strong photothermal effects. In addition, it was determined that the S_n and D_n values should be balanced in order to achieve a high precision sensing performance when designing sensors for surface plasmon resonance applications.

In general, for SPR experiments, the external interference sources, for example, the system noise, temperature effect, and nonspecific binding, may induce cross-sensitivity issues, thereby decreasing the S_n and D_n values of the SPR biosensors. To be specific, the temperature effect is a non-negligible problem for field measurement because a small temperature variation (0.1 °C) has a large influence on the change of the refractive index (1×10^{-5}), which is comparable with the minimum signal for prototype two-channel SPR sensors. Additionally, the plasmon resonance curves will be influenced by the varied optical properties of the Au/dielectric nanointerfaces induced by the photothermal effects, which would change the S_n and D_n values of the SPR biosensors. Therefore, the ambient and sensor temperatures need to remain stable as much as possible during the recording of the measurement results. To eliminate the temperature influences and obtain accurate SPR signals, two effective experimental approaches have been proposed and applied in recent years, as shown in Table S2. First, in major SPR research studies, the reference channel (multi-channel) method has been selected to eliminate the temperature influences (Chen et al., 2016; De Souza Filho et al., 2017; Hong et al., 2018; Wei et al., 2017; Zhang et al., 2017). The reference channel possesses the same external conditions compared to the working channel and therefore provides compensations for the temperature, bulk refractive index, and non-specific binding variations. Second, temperature stabilization (regulation) has also been a feasible approach used to dispose of the temperature factor (Kitagawa et al., 2016; Zhang et al., 2016). It can enormously stabilize the varying ambient temperatures and the critical component temperatures in order to suppress the measurement noise for SPR sensors.

In essence, the above two experimental approaches used to pursue high sensitivity and obtain accurate SPR signals have been focused on eliminating the temperature influences. However, as discussed above, the sensing performances of graphene/Au SPR sensors can be tailored with the temperatures variations, and thus the temperature factor can be utilized to tune the S_n and D_n values of the SPR sensors. In other

words, we are aiming to utilize the temperatures to enhance the sensing performances of the SPR sensors. To pursue higher S_n values, it is reasonable to obtain higher temperatures by tuning the power of incident lights or controlling the experiment temperatures. For the 1L-T stacked graphene/Au SPR sensor, the S_n increased 2.6% when the temperature is increased from 300 K to 500 K. In order to keep the extraordinary D_n values, it was necessary to maintain a lower temperature. For the 1L-T stacked graphene/Au SPR sensor, the D_n has increased 19.4% when the temperature is decreased from 300 K to 100 K. This method could expand the applications of the SPR sensors, which could satisfy the different special requirements (higher S_n or D_n values) in various biomedical fields. Therefore, the multiscale simulation method, which is proposed for the exploration of the photothermal effects and the underlying mechanism of interfacial phenomena, provides an effective method to use in searching for more appropriate biofunctional layer materials. It can also be used as an excellent guideline for the performance enhancement and optimization of commercialized SPR sensors in the fields of analytical chemistry and biomedical.

4. Conclusions

We have investigated the photothermal effects in graphene/Au nanointerfaces and the quantitative influences on sensing performances using a multiscale method that combines the density functional theory and molecular dynamics. The dielectric constants of the Au cubic and triclinic structures possess diverse variation trends as the temperature rises. In addition, the influences of the photothermal effects on 1 L graphene, AA-stacking and AB-stacking multilayered graphene are gradually enhanced. As these diversities are imported into graphene/Au SPR sensors in order to elucidate the photothermal effects at graphene/Au nanointerfaces, the sensitivity and detection accuracy results display different response characteristics and variation ranges when the temperatures are tuned between 0 K and 600 K. In particular, the AA-T and 1L-T graphene/Au stacked SPR systems have relatively high sensitivity and less accuracy loss with strong photothermal effects. We have determined that the AA-T and 1L-T stacked graphene/Au systems possess large available temperature ranges and excellent sensing performances for surface plasmon resonance applications. We have provided the fundamental insights regarding the influences of the photothermal effects and quantitatively verified the necessity of the photothermal heating corrections. Further photothermal effect explorations of the Au nanoparticles or graphene oxide films that may potentially lead to greater sensing efficiency and sensitivity SPR sensors are looking forward to be carried out.

Acknowledgements

This work is co-supported by the Fundamental Research Funds for the Central Universities under Grant No. 106112017CDJQJ128836, the Key Science and Technology Program of Chongqing, China under Grant No. cstc2017shms-zdyfX0028, the Technology innovation and application demonstration project of Chongqing under Grant No. cstc2018jszx-cyzd0587, the National Natural Science Foundation of China under Grant No. 51303033, and the Guangxi Natural Science Foundation under Grant No. 2014GXNSFCB118004.

Appendix A. Supporting information

Supplementary data associated with this article can be found in the online version at doi:10.1016/j.bios.2018.11.007.

References

Abadian, P.N., Kelley, C.P., Goluch, E.D., 2014. Anal. Chem. 86, 2799–2812.
Adachi, S., 2012. World Sci.
Amendola, V., 2016. Phys. Chem. Chem. Phys. 18, 2230–2241.
Blöchl, P.E., 1994. Phys. Rev. B 50, 17953.
Çakır, D., Sahin, H., Peeters, F.M., 2014. Phys. Rev. B 90, 205421.
Calizo, I., Balandin, A., Bao, W., Miao, F., Lau, C., 2007. Nano Lett. 7, 2645–2649.
Chen, S., Liu, Y., Liu, Q., Peng, W., 2016. IEEE Photon Technol. Lett. 28, 213–216.
Chen, X., Chen, Y., Yan, M., Qiu, M., 2012. ACS Nano 6, 2550–2557.
De Souza Filho, C.A., Lima, A.M.N., Neff, F.H., 2017. IEEE Sens. J. 17, 6246–6257.
Falkovsky, L., 2008. J. Phys.: Conf. Ser. 129, 012004.
Falkovsky, L., Pershoguba, S., 2007. Phys. Rev. B 76, 153410.
Flores, M.Z., Autreto, P.A., Legoas, S.B., Galvao, D.S., 2009. Nanotechnology 20, 465704.
Foiles, S., Baskes, M., Daw, M.S., 1986. Phys. Rev. B 33, 7983.
Galvez, F., de Lara, D.P., Spottorno, J., García, M., Vicent, J., 2017. Sens. Actuators B: Chem. 243, 806–811.
Homola, J., 2003. Anal. Bioanal. Chem. 377, 528–539.
Hong, L., Lu, M., Dinel, M.-P., Blain, P., Peng, W., Gu, H., Masson, J.-F., 2018. Biosens. Bioelectron. 109, 230–236.
Iyer, G.R.S., Wang, J., Wells, G., Guruvenket, S., Payne, S., Bradley, M., Borondics, F., 2014. ACS Nano 8, 6353–6362.
Jain, A., Hautier, G., Moore, C.J., Ong, S.P., Fischer, C.C., Mueller, T., Persson, K.A., Ceder, G., 2011. Comput. Mater. Sci. 50, 2295–2310.
Kim, S., Lee, H.J., 2015. Anal. Chem. 87, 7235–7240.
Kitagawa, S., Yamazaki, H., Hosoki, A., Nishiyama, M., Watanabe, K., 2016. Photon. Instrum. Eng. III 9754, 97541B.
Kresse, G., Furthmüller, J., 1996. Comput. Mater. Sci. 6, 15–50.
Kretschmann, E., 1971. Z. Für Phys. A Hadrons Nucl. 241, 313–324.
Kumar Maharana, P., Bharadwaj, S., Jha, R., 2013. J. Appl. Phys. 114, 014304.
Lahav, A., Auslender, M., Abdulhalim, I., 2008. Opt. Lett. 33, 2539–2541.
Lee, C., Wei, X., Kysar, J.W., Hone, J., 2008. Science 321, 385–388.
Liu, C., Cohen, J., Adams, J., Voter, A., 1991. Surf. Sci. 253, 334–344.
Liu, Z., Chen, H., Jia, Y., Zhang, W., Zhao, H., Fan, W., Zhang, W., Zhong, H., Ni, Y., Guo, Z., 2018. Nanoscale.
Maharana, P.K., Jha, R., 2012. Sens. Actuators B: Chem. 169, 161–166.
Melchionna, S., Ciccotti, G., Lee Holian, B., 1993. Mol. Phys. 78, 533–544.
Miao, J., Hu, W., Jing, Y., Luo, W., Liao, L., Pan, A., Wu, S., Cheng, J., Chen, X., Lu, W., 2015. Small 11, 2392–2398.
Mohammadzadeh-Asl, S., Keshtkar, A., Dolatabadi, J.E.N., de la Guardia, M., 2018. Biosens. Bioelectron. 101, 118–131.
Morgan, W., 1972. Carbon 10, 73–79.
Mounet, N., Marzari, N., 2005. Phys. Rev. B 71, 205214.
Naimushin, A.N., Soelberg, S.D., Bartholomew, D.U., Elkind, J.L., Furlong, C.E., 2003. Sens. Actuators B: Chem. 96, 253–260.
Nelson, J., Daw, M., Sowa, E.C., 1989. Phys. Rev. B 40, 1465.
Nenninger, G., Tobiška, P., Homola, J., Yee, S., 2001. Sens. Actuators B: Chem. 74, 145–151.
Nix, F., MacNair, D., 1941. Phys. Rev. 60, 597.
O'Brien II, M.J., Brueck, S., Perez-Luna, V.H., Tender, L.M., Lopez, G.P., 1999. Biosens. Bioelectron. 14, 145–154.
Pang, J., Yang, Q., Ma, X., Wang, L., Tan, C., Xiong, D., Ye, H., Chen, X., 2017. Phys. Chem. Chem. Phys. 19, 30852–30860.
Pavone, P., Karch, K., Schütt, O., Strauch, D., Windl, W., Giannozzi, P., Baroni, S., 1993. Phys. Rev. B 48, 3156.
Plimpton, S., Crozier, P., Thompson, A., 2007. Scandia Natl. Lab. 18 (43-43).
Qiu, J., Wei, W.D., 2014. J. Phys. Chem. C 118, 20735–20749.
Quereda, J., San-Jose, P., Parente, V., Vaquero-Garzon, L., Molina-Mendoza, A.J., Agraït, N., Rubio-Bollinger, G., Guinea, F., Roldán, R., Castellanos-Gomez, A., 2016. Nano Lett. 16, 2931–2937.
Raether, H., 1988.
Reimhult, E., Höök, F., Kasemo, B., 2003. Langmuir 19, 1681–1691.
Röntzsch, L., Heinig, K.-H., Schuller, J.A., Brongersma, M.L., 2007. Appl. Phys. Lett. 90, 044105.
Roper, D.K., Ahn, W., Hoepfner, M., 2007. J. Phys. Chem. C 111, 3636–3641.
Saha, S.K., Waghmare, U., Krishnamurthy, H., Sood, A., 2008. Phys. Rev. B 78, 165421.
Santos, E.J., Kaxiras, E., 2013. Nano Lett. 13, 898–902.
Schasfoort, R.B., 2017. R. Soc. Chem.
Singh, M., Holzinger, M., Tabrizian, M., Winters, Sa, Berner, N.C., Cosnier, S., Duesberg, G.S., 2015. J. Am. Chem. Soc. 137, 2800–2803.
Song, B., Li, D., Qi, W., Elstner, M., Fan, C., Fang, H., 2010. ChemPhysChem 11, 585–589.
Stebunov, Y.V., Aftenieva, O.A., Arsenin, A.V., Volkov, V.S., 2015. ACS Appl. Mater. Interfaces 7, 21727–21734.
Stern, D., Pauly, D., Zydek, M., Müller, C., Avondet, M.A., Worbs, S., Lisdat, F., Dorner, M.B., Dorner, B.G., 2016. Biosens. Bioelectron. 78, 111–117.
Süle, P., Szendrő, M., Hwang, C., Tapasztó, L., 2014. Carbon 77, 1082–1089.
Tan, C., Yang, Q., Meng, R., Liang, Q., Jiang, J., Sun, X., Ye, H., Chen, X., 2016. J. Mater. Chem. C 4, 8171–8178.
Taylor, A.D., Ladd, J., Yu, Q., Chen, S., Homola, J., Jiang, S., 2006. Biosens. Bioelectron. 22, 752–758.
Tsang, D., Marsden, B., Fok, S., Hall, G., 2005. Carbon 43, 2902–2906.
Wang, Q., Li, Q., Yang, X., Wang, K., Du, S., Zhang, H., Nie, Y., 2016. Biosens. Bioelectron. 77, 1001–1007.
Wei, Y., Su, Y., Liu, C., Nie, X., Liu, Z., Zhang, Y., Zhang, Y., 2017. Sensors 17, 2862.
Xu, Y., Li, X., Dong, J., 2010. Nanotechnology 21, 065711.
Xue, T., Cui, X., Chen, J., Liu, C., Wang, Q., Wang, H., Zheng, W., 2013. ACS Appl. Mater. Interfaces 5, 2096–2103.
Xue, T., Cui, X., Guan, W., Wang, Q., Liu, C., Wang, H., Qi, K., Singh, D.J., Zheng, W., 2014. Biosens. Bioelectron. 58, 374–379.
Yang, Q., Meng, R.-S., Jiang, J.-K., Liang, Q.-H., Tan, C.-J., Cai, M., Sun, X., Yang, D.-G.,

Ren, T.-L., Chen, X.-P., 2016. IEEE Electron Device Lett. 37, 660–662.
Yang, S., Wang, C., Sahin, H., Chen, H., Li, Y., Li, S.-S., Suslu, A., Peeters, F.M., Liu, Q., Li, J., 2015. Nano Lett. 15, 1660–1666.
Yoon, D., Son, Y.-W., Cheong, H., 2011. Nano Lett. 11, 3227–3231.
Yue, Y., Zhang, Q., Zhang, X., Yang, Z., Yin, P., Guo, L., 2017. Small 13.
Zakharchenko, K., Los, J., Katsnelson, M.I., Fasolino, A., 2010. Phys. Rev. B 81, 235439.
Zeng, S., Baillargeat, D., Ho, H.-P., Yong, K.-T., 2014. Chem. Soc. Rev. 43, 3426–3452.
Zeng, S., Hu, S., Xia, J., Anderson, T., Dinh, X.-Q., Meng, X.-M., Coquet, P., Yong, K.-T., 2015a. Sens. Actuators B: Chem. 207, 801–810.
Zeng, S., Sreekanth, K.V., Shang, J., Yu, T., Chen, C.K., Yin, F., Baillargeat, D., Coquet, P., Ho, H.P., Kabashin, A.V., 2015b. Adv. Mater. 27, 6163–6169.
Zhang, P., Liu, L., He, Y., Ji, Y., Guo, J., Ma, H., 2016. Plasmonics 11, 771–779.
Zhang, X.-l., Liu, Y., Fan, T., Hu, N., Yang, Z., Chen, X., Wang, Z.-y., Yang, J., 2017. Sensors 17, 1435.
Zhao, S.S., Bukar, N., Toulouse, J.L., Pelechacz, D., Robitaille, R., Pelletier, J.N., Masson, J.-F., 2015. Biosens. Bioelectron. 64, 664–670.